Title

Un-collimated single-photon imaging system for high-sensitivity small animal and plant imaging

Journal

Physics in Medicine and Biology, 60(1)

ISSN

0031-9155

Authors

Walker, Katherine L
Judenhofer, Martin S
Cherry, Simon R
et al.

Publication Date

2015-01-07

DOI

10.1088/0031-9155/60/1/403

Peer reviewed

HHS Public Access

Author manuscript

Phys Med Biol. Author manuscript; available in PMC 2016 January 07.

Published in final edited form as:

Phys Med Biol. 2015 January 7; 60(1): 403–420. doi:10.1088/0031-9155/60/1/403.

Un-collimated single-photon imaging system for high-sensitivity small animal and plant imaging

Katherine L. Walker, **Martin S. Judenhofer**, **Simon R. Cherry**, and **Gregory S. Mitchell**

Department of Biomedical Engineering, University of California, Davis, One Shields Avenue, Davis, CA 95616, USA

Katherine L. Walker: klbyrne@ucdavis.edu

Abstract

In preclinical single-photon emission computed tomography (SPECT) system development the primary objective has been to improve spatial resolution by using novel parallel-hole or multi-pinhole collimator geometries. However, such high-resolution systems have relatively poor sensitivity (typically 0.01% to 0.1%). In contrast, a system that does not use collimators can achieve very high-sensitivity. Here we present a high-sensitivity un-collimated detector single-photon imaging (UCD-SPI) system for the imaging of both small animals and plants. This scanner consists of two thin, closely spaced, pixelated scintillator detectors that use NaI(Tl), CsI(Na), or BGO. The performance of the system has been characterized by measuring sensitivity, spatial resolution, linearity, detection limits, and uniformity. With ^{99m}Tc (140 keV) at the center of the field of view (20 mm scintillator separation), the sensitivity was measured to be 31.8% using the NaI(Tl) detectors and 40.2% with CsI(Na). The best spatial resolution (FWHM when the image formed as the geometric mean of the two detector heads, 20 mm scintillator separation) was 19.0 mm for NaI(Tl) and 11.9 mm for CsI(Na) at 140 keV, and 19.5 mm for BGO at 1116 keV, which is somewhat degraded compared to the cm-scale resolution obtained with only one detector head and a close source. The quantitative accuracy of the system's linearity is better than 2% with detection down to activity levels of 100 nCi. Two *in vivo* animal studies (a renal scan using ^{99m}Tc MAG-3 and a thyroid scan with ^{123}I) and one plant study (a $^{99m}TcO_4^-$ xylem transport study) highlight the unique capabilities of this UCD-SPI system. From the renal scan, we observe approximately a one thousand-fold increase in sensitivity compared to the Siemens Inveon SPECT/CT scanner. UCD-SPI is useful for many imaging tasks that do not require excellent spatial resolution, such as high-throughput screening applications, simple radiotracer uptake studies in tumor xenografts, dynamic studies where very good temporal resolution is critical, or *in planta* imaging of radioisotopes at low concentrations.

Keywords

Sensitivity; SPECT; Small Animal Imaging; Plant Imaging

1. Introduction

In preclinical single-photon emission computed tomography (SPECT) system development, the small size of the murine model and its organs has motivated work to improve system spatial resolution [e.g. Erlandsson 1993, Ishizu 1993, Jaszczak 1994, Acton and Kung 2003,

Beekman 2005, van der Have 2009]. Spatial resolution is primarily governed by the collimator design, with very high resolution achievable with small-diameter pinhole collimation [Jaszczak 1994]. However, when the pinhole apertures are small, the radiation flux that can reach the detectors is reduced, thereby decreasing the sensitivity, where sensitivity is defined as the fraction of emitted gamma-rays detected by the system. Therefore, the consequence of developing SPECT systems with very high spatial resolution is relatively poor sensitivity [Meikle 2005, Loudos 2003, Cherry 2004, Bradley 2006, Beekman and van der Have 2007, Magota 2011].

Preclinical SPECT imaging systems with sub-millimeter spatial resolution have sensitivity less than 0.3%, more typically in the range of 0.01% to 0.1% [Jansen 2007, Rowland 2008]. When imaging with such systems, one can compensate for poor system sensitivity either by employing long imaging times or by administering a high radiation dose. The former affects throughput and limits the imaging of fast dynamic processes, while the latter may increase the cost of radioisotope for the study and introduce confounding radiation exposure effects for the subject, especially for long-lived isotopes. To improve the sensitivity of SPECT systems, multiple pinholes [van der Have 2009] or coded apertures [Meikle 2001, Mu 2009] may be used. Nonetheless, sensitivities are still well under 1% and, due to overlapping projection information, the effective sensitivity may be even lower.

There are specific imaging tasks where high sensitivity is advantageous and, in fact, preferred over excellent spatial resolution. Examples requiring high sensitivity include, but are not limited to, the following: i) high-throughput preclinical screening applications; ii) counting of radiolabeled cells *in vitro*; iii) *in vivo* imaging of easily saturated receptor systems; or iv) *in planta* dynamic material transport imaging of radioisotopes at low concentrations. One very common preclinical molecular imaging application is uptake and kinetics of biodistribution of novel radiotracers or labeled therapeutic agents in superficial tumor xenografts in mice. Radiotracer studies in plants also offer opportunities. The biodistribution of a radiolabeled compound is typically analyzed by plant dissection and counting in a well counter and for β- emitters, by ashing the plants' tissues and counting them with a liquid scintillator counter; however with these approaches, many studies of interest such as dynamic material transport and sequestration studies are not feasible. Although a relatively unexplored area of plant research, whole plant organism imaging would facilitate large-scale material transport studies and potentially allow each subject to be its own control [Jahnke 2009, Wang 2014].

A nuclear imaging system with very high sensitivity permits faster image acquisition thereby facilitating rapid dynamic imaging, and requires less administered radioactive tracer. An example of a preclinical nuclear imaging system designed for high-sensitivity applications was our prototype un-collimated detector single-photon imaging system [Mitchell 2009]. This system achieved 40% sensitivity with ^{99m}Tc and 3 mm thick monolithic NaI(Tl) detectors, which is more than a one hundred-fold increase in sensitivity compared to existing preclinical SPECT scanners [Rowland 2008]. Dynamic *in vivo* scans with this system show that un-collimated detector single-photon imaging provides useful molecular imaging information, even when using very low amounts of injected radioactivity. The construction of the second-generation un-collimated detector single-photon imaging

(UCD-SPI) system was motivated by limitations identified in the prototype system, including the inflexible gantry construction (restricting its use to small animal imaging), its small area of uniform response (producing undesirable edge effects), and its poor sensitivity at higher gamma-ray energies.

The conceptual design of the UCD-SPI system is shown in figure 1. It consists of two detector heads (indicated in red) housing thin scintillator arrays, and two dual-axis motion stages. With narrow detector spacing, large solid angle coverage and high sensitivity is achieved. For thin imaging subjects such as mice and small plants, coarse images can be formed by using solid angle effects alone, thereby eliminating the need for a collimator. With respect to small animal imaging, the dual-axis motion stages facilitate easy positioning of the imaging subject on the lower detector (figure 1 (a)). The upper detector is then precisely aligned immediately above the opposing lower detector (figure 1(b,c)). With respect to small plant imaging, in order to keep the plant in its natural vertical orientation during imaging, the system can be rotated 90° on its side (figure 1(d)). The plant can be moved vertically through the system's field of view (FOV) to image its full extent. Furthermore, the flexible design of the detector heads offers the ability to interchange arrays of different scintillator materials, so as to optimize detection efficiency for a wide range of isotopes emitting different gamma-ray energies.

In this work the development and characterization of the UCD-SPI system is presented. The performance of this scanner was characterized by its sensitivity, spatial resolution, linearity and detection limits, as well as uniformity. Additionally, the imaging capabilities for both small animals and plants are demonstrated with a dynamic *in vivo* renal scan, an *in vivo* thyroid blocking study, and a dynamic *in planta* study of xylem transport.

2. Materials and Methods

2.1. System Description

Photographs of the mechanical structure and housing of the UCD-SPI system are shown in figure 2 for both the small animal and plant configurations. The components of the scanner include: two detector boxes made from Delrin, mechanical support rods (47065T101, McMaster-Carr, Los Angeles, CA, USA), custom built manual and motorized slides (Velmex, Bloomfield, NY, USA), and a camera (HD Webcam C525, Logitech, Newark, CA, USA). The webcam takes photographs of the imaging subject, which are later co-registered with the imaging data, giving an anatomical or physical reference similar to that provided in most small animal optical imaging systems. The size of the scintillator detectors (5 cm × 10 cm) allows for a whole mouse to be easily imaged in one acquisition, but multiple acquisitions would be required to image an entire, full grown *Arabidopsis* plant (~30 cm tall). Therefore, a separate gantry has been constructed that can move a plant through the FOV for whole plant imaging.

Each detector head contains one pixelated, scintillator detector array, coupled to two Hamamatasu H8500 multi-channel position-sensitive photomultiplier tubes (MCPMTs), that are mounted on two printed circuit boards [Walker 2014]. Available scintillator arrays include: 3 mm thick thallium-doped sodium iodide (NaI(Tl)) detectors, 3 mm thick sodium-

doped cesium iodide (CsI(Na)) detectors, and 5 mm thick bismuth germanate (BGO) detectors. The scintillator arrays can be selected based upon the imaging study to maximize system sensitivity. The NaI(Tl) arrays were manufactured by Saint-Gobain (Cleveland, OH, USA); arrays of two different pixel dimensions were selected, 1.5 mm × 1.5 mm (1.7 mm pitch) and 2 mm × 2 mm (2.2 mm pitch). Two CsI(Na) arrays with identical pixel dimensions were manufactured by Hilger (Margate, Kent, United Kingdom), 1.5 mm × 1.5 mm (1.6 mm pitch). The two BGO arrays, manufactured by Proteus (Chagrin Falls, OH, USA), were also identical in pixel size (1.92 mm × 1.92 mm on a 2 mm pitch).

The data acquisition (DAQ) system consists of standard nuclear instrumentation modules (figure 3). The eight raw signals from each detector are fed through a 16-channel amplifier (778, Phillips Scientific, Mahwah, NJ, USA) to be split into a triggering and energy branch. In the triggering branch, eight signals are combined in a fan-in-out unit (740, Phillips Scientific) to provide one summed signal per detector which is processed by a fast filter amplifier (FFA) (579, Ortec, Oak Ridge, TN, USA), and then sent to a constant fraction discriminator (CFD) (584, Ortec) to provide a logic gate for each of the two detector heads. When one of the 14-bit precision 8-channel DAQ boards (UEI PowerDAQ, Walpole, MA, USA) is triggered by the delayed CFD signal from a gate & delay unit (G&D) (416, Ortec), all eight channels from the energy branch are digitized after passing them through a shaping amplifier (N568B, CAEN, Staten Island, NY, USA). Both DAQ boards are read out with a single computer running custom software [Judenhofer 2005]. The two boards run asynchronously but are accompanied by a time stamp file to correspond each buffer read to the system clock. Anger logic equations are used to recover the location of the detected event in the scintillator [Walker 2014]. Counting rate performance is dominated by the data acquisition system, which has been previously characterized as fitting a nonparalyzable model with a dead time of 4.35 μs [Judenhofer 2005, Walker 2014].

2.2. Performance Characterization

All performance characterization measurements were made with scintillator-to-scintillator detector spacing of 20 mm. This detector separation was selected since the height of a prone, anesthetized, 25 g mouse is ~15 mm. Due to detector packaging on the front face of the scintillators, a 20 mm scintillator spacing is the closest detector separation which can still comfortably fit a small animal for imaging.

2.2.1. Sensitivity—As sensitivity is the critical performance parameter for this un-collimated nuclear imaging technique, experimental measurements were also compared against Monte Carlo simulations to ensure that there were no significant event losses in the system and that the predicted sensitivity was achieved for different detector configurations and source energies.

First, the sensitivity profile of the system was measured using 1 μCi of ^{99m}Tc translated in 10 mm increments along the axial direction between the two NaI(Tl) scintillator detectors. The axial direction is the axis parallel to the detector faces and is the longer dimension of the scintillator arrays. The sensitivity at each location was determined as the percentage of emitted gamma-rays detected by the system with a 40% energy window about the

photopeak. Experimental results were compared to simulations performed using GATE with a 140 keV monoenergetic source and NaI(Tl) scintillators of the same thickness, pixel size and pitch, and configuration as in the experimental setup. The same energy window was used for the GATE simulations. Simulation results were corrected for the 89% branching ratio of ^{99m}Tc, meaning the sensitivity numbers predicted from simulations of a monoenergetic source were multiplied by 0.89 before including in figure 4 or table 1.

Subsequently, the sensitivity in the center of the field of view (CFOV) was evaluated experimentally and compared to GATE using a wide energy range of monoenergetic gamma-ray sources and all scintillator arrays. A 40% energy window about the photopeak was applied to both sets of data. In all cases, the GATE simulation data was corrected for the appropriate branching ratios of the radionuclides used experimentally. Since the NaI(Tl) detectors produce flood histograms of good quality with low to mid-energy isotopes [Walker 2014], ^{109}Cd (22 keV) and ^{99m}Tc (140 keV) were evaluated. Mid to high-energy isotopes, ^{99m}Tc and ^{65}Zn (1116 keV), were used with the CsI(Na) array. Due to the higher stopping power and lower light yield of the BGO array, ^{65}Zn was selected for measuring its sensitivity.

The detectors were modeled in GATE with the same pixel size and pitch as in the experimental setup. For the 3 mm thick NaI(Tl) scintillators, two different sized arrays were simulated, one for the upper detector and the other for the lower detector: a 24 × 51 array of pixel size 1.5 mm × 1.5 mm (1.7 mm pitch) and a 21 × 41 array of 2 mm × 2 mm pixels (2.2 mm pitch). For the 3 mm thick CsI(Na) arrays, the upper and lower detector arrays were sized identically (28 × 56 array of pixel size 1.5 mm × 1.5 mm, on a 1.6 mm pitch). For the 5 mm thick BGO arrays, both the upper and lower detector arrays were also sized identically (25 × 50 array of pixel size 1.92 mm × 1.92 mm, on a 2 mm pitch). For all simulations, the gaps between the pixels were modeled as air (the arrays used experimentally have an unspecified reflector material between the pixels). Additionally, a 0.5 mm thick aluminum entrance window was simulated in GATE in front of the scintillator arrays.

2.2.2. Spatial Resolution—The intrinsic system spatial resolution was measured with a capillary tube filled with 1 μCi activity and placed between the scintillator detectors. ^{99m}Tc was used to fill the capillary tube for the measurements made with both the NaI(Tl) and CsI(Na) detectors, and a ^{65}Zn-filled capillary tube was used for the measurements made with the BGO array. In order to assess how spatial resolution changes as a function of distance normal to the detector surface, measurements were made at various source distances between the opposing scintillator detector heads. For each measurement, the two detector head projection images were combined into a single image using the geometric mean. The geometric mean is useful because it has less depth dependence on the location of the source between the two detectors (than the arithmetic mean) for the quantitative accuracy of the combined signal. The spatial resolution was determined as the FWHM of the line profiles through the image of the capillary.

2.2.3. Linearity and Detection Limits—To determine the system's linearity and detection limits, four wells of a 96-well plate were filled with four different activities of ^{99m}Tc solution: 100 nCi, 200 nCi, 400 nCi, and 800 nCi. The relative activities of the four

wells are estimated to be accurate to better than ±1%, as they were obtained by dilution from a common solution. Each well was filled with 100 μL of the various radioactive solution activities, which corresponds to a well height of approximately 4 mm. The 96-well plate was imaged for 10 min using the pixelated NaI(Tl) scintillator detectors. Due to the shallow height of radioactive solution in each well and the well plate thickness, the image from the lower detector (closest to the radioactivity) yielded significantly better spatial resolution compared to the image from the upper detector. To determine system linearity, the number of counts from each well was summed (using a 10 pixel × 10 pixel ROI from the image of the lower detector) and plotted versus known activity.

2.2.4. Uniformity—Uniformity was determined from two 10 h acquisitions of flood images with a 100 μCi source located 50 cm from one of the detector heads. Counts were recorded for events falling within a 40% energy window about the photopeak. The energy window was applied on a crystal-by-crystal basis. For both the NaI(Tl) and CsI(Na) scintillators, the 122 keV photopeak of ^{57}Co was used, and for BGO the 1116 keV photopeak of ^{65}Zn was used.

The first acquired image was used to create the detector normalization file, by which the second image was subsequently corrected. A 3 × 3 smoothing filter was applied to both the uncorrected and flood-corrected images, and the integral and differential uniformity were calculated for the useful field of view (UFOV) according to the NEMA standard [NEMA 2007]. The UFOV is the area of the detector used for gamma-ray imaging, which is the entire array minus two pixels at the edge. The integral uniformity is the difference between the maximum and the minimum pixels, divided by the sum of these two values, and then multiplied by 100 [NEMA 2007]. The differential uniformity was calculated using the two pixels with the largest difference within a set of 5 contiguous pixels (in a row or column) and the same formula as integral uniformity [NEMA 2007].

2.3. Animal Experiments

Animal studies were conducted according to an approved animal use protocol at the University of California, Davis. The NaI(Tl) scintillator detectors were selected for both animal imaging studies based on the energy of the radioisotopes used (^{99m}Tc = 140 keV, ^{123}I = 159 keV).

2.3.1. In vivo Renal Scan—To demonstrate the potential for rapid dynamic imaging, the ^{99m}Tc labeled radiotracer mercaptoacetyltriglycine (MAG-3) was selected, which is a renal imaging probe that moves from the bloodstream through the kidneys to the bladder over the course of several minutes [Maini 1989, Roberts 2007]. One healthy adult (39 g) BALB/c mouse received a 5 μCi injection of ^{99m}Tc MAG-3 (intravenous injection with 50 μL saline flush) on the scanner, with the scintillators separated by 25 mm. The mouse was imaged continuously for 25 mins. 45 mins post injection the same mouse was scanned on a commercial SPECT/CT scanner (Siemens Inveon), using the 5-pinhole mouse whole-body collimator (1 mm diameter pinholes) for 30 min. The image was acquired over 60 projection angles, for 25 s per angle.

2.3.2. In vivo Thyroid Imaging—As an example of using the UCD-SPI system for screening/biodistribution applications with very low doses of radioactivity, ^{123}I and nonradioactive potassium iodide (KI) were used in a blocking study. Once introduced *in vivo*, ^{123}I is actively transported into the thyroid by the sodium iodide symporter [Hammond 2007]. Thyroid uptake of radioactive iodine can be reduced if, before exposure, nonradioactive iodine is administered (e.g. KI or NaI). Blocking the thyroid from radioisotope exposure prevents many harmful side effects, especially in children [Cardis 2005].

The effectiveness of various blocking doses of KI prior to ^{123}I exposure in mice was evaluated. All BALB/c mice were healthy, with weights ranging between 18–21 g (19.4 ± 1.42 g). Two treatment groups received 1× (2.25 μg/g) and 10× (22.5 μg/g) human equivalent blocking doses of KI. The selected KI blocking dose was administered (intraperitoneal injection) 60 min prior to ^{123}I (intravenous injection with 50 μL saline flush). As a control, another group did not receive any KI treatment. For all scans the mice were injected with only 3 μCi ^{123}I and imaged continuously for the first 20 min after injection, and at the 6 h and 24 h time points thereafter. For all scans, the entrance faces of the scintillators were separated by 20 mm.

2.4. Plant Experiment

To demonstrate the capability of the system for plant imaging, ^{99m}Tc pertechnetate ($^{99m}TcO_4^-$) was selected. $^{99m}TcO_4^-$ is extracted by plant roots, transported in the xylem, and accumulated in the leaves because ^{99m}Tc is not evaporated [Currie 2010]. Two-week-old sunflower plants (germinated in soil and then transferred to hydroponic nutrient solutions) were incubated in 250 mL of a 10 mCi/L $^{99m}TcO_4^-$ solution for 15 min. The roots in direct contact with the radioactive solution were rinsed with nutrient solution 3× prior to imaging. Then the plants were placed in a hydroponic solution without any radioisotope and isotope uptake was dynamically imaged on the UCD-SPI system for 45 min. The entrance faces of the scintillators were separated by 20 mm due to the thickness of the plant holder. The final image was made using the detector closest to the plant stem since it had better spatial resolution compared to the image formed using the geometric mean of both detector heads.

3. Results

3.1. Performance Characterization

3.1.1. Sensitivity—Figure 4 shows the axial sensitivity profile of the system for ^{99m}Tc using the NaI(Tl) detectors. At the CFOV the experimental and GATE simulation measurements agree within 5%. Due to the un-collimated detectors, when the source is outside of the FOV of the scanner (outside the ±45 mm lines) the sensitivity is nonzero (~6% sensitivity 15 mm outside the FOV).

Table 1 presents the experimental and GATE sensitivity results at the CFOV for all scintillator materials and radionuclides evaluated. The values for experimental and simulation sensitivities agree within a few percent showing that there are no significant

event losses in the system. For all measurements the simulated sensitivity in GATE is slightly higher than the experimentally measured sensitivity. These differences are most likely due to uncertainties in the materials used to package the detectors, the reflector material used between scintillator pixels, the finite energy resolution which introduces uncertainties in the lower threshold, and small amounts of electronic dead time.

3.1.2. Spatial Resolution—The spatial resolution (FWHM) from the capillary tube measurements, and using the geometric mean to combine the two detector heads' data, is shown in figure 5(a); here the spatial resolution is presented as a function of distance from one scintillator detector. The best spatial resolution is achieved when the capillary tube is touching one detector head: 19.0 mm for the NaI(Tl) detectors, 11.9 mm for the CsI(Na) detectors, and 19.5 mm for the BGO detectors. This illustrates the importance of minimizing the detector packaging in front of the scintillator array. For a given source location, the CsI(Na) arrays have the best spatial resolution since these arrays have the smallest pixel size of all arrays evaluated (1.5 mm × 1.5 mm, 1.6 mm pitch) while the BGO arrays have the worst spatial resolution for each source location due to the higher energy gamma-rays imaged and the thickness of the detector material (5 mm). For all detectors, the FWHM rapidly degrades with increased distance from the detector face, reaching a maximum value of ~2.5 for the CsI(Na) detectors and ~3.5 cm for the BGO detectors at 10 mm which corresponds to the CFOV.

Using the lower and upper detector images individually, rather than forming the geometric mean, yields improved spatial resolution for the detector closest to the source. In figure 5(b) the FWHM measured for each individual CsI(Na) detector head is shown along with the combined geometric mean from both detector heads. 7.5 mm FWHM is measured at the aluminum entrance window for the lower detector (1.5 mm from the scintillator face). For the upper detector, the data for the capillary tube when positioned close to the lower detector are omitted since at these locations the radioactivity was nearly uniformly distributed on the detector and the FWHM not clearly measurable. With the NaI(Tl) detectors, slightly worse (due to detector packaging) but still cm-scale resolution is measured with the use of only one detector head, for sources very close to the entrance window [Walker 2014].

3.1.3. Linearity and Detection Limits—The image in figure 6(a) shows the system's ability to resolve four wells in a 96-well plate containing trace amounts of ^{99m}Tc solution. For each well, the number of detected counts in a 10 × 10 pixel ROI was summed and plotted in figure 6(b). From a linear fit to the data, the amount of activity in each well was determined to deviate from the best-fit line by no more than ±2% (figure 6(c)). The response of the system is linear over the 100 nCi to 1 μCi range, enabling the UCD-SPI system to quantitatively detect sub μCi levels of activity with a detection limit <100 nCi.

3.1.4. Uniformity—Table 2 presents the integral and differential uniformity values for both the uncorrected and corrected detector images, for all scintillator materials. The integral uniformity is better than 3% for all arrays after correction and the differential uniformity is better than 1%. The uncorrected integral uniformity for the CsI(Na) array is significantly higher than the other arrays not because of non-uniformities in the scintillator material itself

but rather because of the poor light collection in the gap between the two MCPMTs. This is primarily attributable to the thinner optical window that reduces light spreading.

3.2. Animal Experiments

3.2.1. In vivo Renal Scan—The upper and lower detector head images from the ^{99m}Tc MAG-3 scan were thresholded and overlaid on a photograph of the mouse (figure 7(a)). Each frame represents just 2 s of data, beginning at 0 s, 10 s, 2 min, 3 min, 5 min, and 10 min after injection. The average system count rate (sum of two detector heads) over the 25 min scan was 54 kcps with a peak count rate of 66 kcps. The images from ~2–5 min show radiotracer drainage from the kidneys into the bladder. At 10 min a majority of the radiotracer is localized in the bladder.

Two square ROIs are indicated in the images furthest on the left of figure 7(a): the blue square denotes the kidneys which are located dorsally (closer to the upper detector) and the red square indicates the bladder which is located ventrally (closer to the lower detector). The average value within each ROI versus time is plotted in figure 7(b), showing the time dependence of the ^{99m}Tc MAG-3 distribution in the mouse. Images were binned in 2 s intervals for this plot, showing the excellent temporal resolution that high-sensitivity imaging permits. When the same mouse was scanned on the Siemens Inveon SPECT/CT scanner 45 min post injection, the count rate was just 15 cps. This is approximately a one thousand-fold decrease in sensitivity compared to the UCD-SPI system. In addition, the radiotracer was shown to have localized in the bladder on the Siemens Inveon scanner, consistent with the last frame of figure 7(a) at 10 min.

3.2.2. In vivo Thyroid Imaging—Figure 8 shows the geometric mean of the co-registered detector images for the mice injected with 3 μCi ^{123}I, thresholded and overlaid on photographs of the mice. At 6 h post injection, the radioisotope distribution is nominally identical for all mice and the radioactivity in the thyroid cannot be visualized clearly. However, at 24 h post injection, radiotracer accumulation in the thyroid occurs only for the mouse that did not receive any KI blocking dose and there is no appreciable difference in thyroid blocking for the 1× and 10× blocking dosages.

3.3. Plant Experiment

Figure 9 shows thresholded $^{99m}TcO_4^-$ images from one detector head of the UCD-SPI system overlaid on a photograph of the plant. The images shown are significantly thresholded to allow the underlying photograph to be visible and to emphasize the areas of most concentrated radioisotope uptake. The average system count rate during the scan was 2 kcps. Each frame represents 45 s of data, beginning at 0 min, 1 min, 5 min, 15 min, and 30 min after plant incubation in radioactive solution and the final nutrient water rinse. The images from ~0–5 min show transport of the tracer from the roots through the xylem and to the leaves. Since imaging was conducted in the dark for better detector performance, transport of the radioactive solution through the xylem is due to residual water potential rather than active transpiration. Four square ROIs are indicated in the far left image of figure 9(a): the gray square is in the root region, the green square is in the lower stem, the red square is in the upper stem, and the blue square is in the apical meristem just below the

leaves. The average value within each ROI versus time is plotted in figure 9(b), showing the time dependence of the $^{99m}TcO_4^-$ distribution in the plant.

4. Discussion and Conclusions

In this work an un-collimated single-photon imaging system has been constructed demonstrating exceptionally high-sensitivity performance unparalleled by other preclinical nuclear imaging systems. This system has potential for many imaging tasks which do not require excellent spatial resolution, for example: high-throughput screening applications, dynamic studies where very good temporal resolution is critical [Celler 2000, Mitchell 2009], counting of radiolabeled cells *in vitro*, *in vivo* imaging of easily saturated receptor systems [Kenanova 2009], or *in planta* imaging of radioisotopes at low concentrations.

Rather than comparing the UCD-SPI system with sophisticated high-resolution multi-pinhole preclinical SPECT systems, a more appropriate point of reference would be to consider this system to be a nuclear imaging analog of optical systems used for *in vivo* bioluminescence or fluorescence imaging [Virostko 2007, Zinn 2008]. While these optical imaging systems have high-sensitivity, they demonstrate poor spatial resolution (limited by light scatter). Typically optical imaging results in semi-quantitative, non-tomographic images in units of photons/mm^2/s that are thresholded and superimposed on a photograph of the mouse. Such systems have found broad utility in a wide array of molecular imaging tasks [Contag 2002, Badr 2011]. Although UCD-SPI produces data similar to optical imaging, it also takes advantage of the wide array of biomolecules and therapeutics that can be radiolabeled, thereby expanding the scope of molecular and metabolic imaging.

One innovation of this UCD-SPI system is the flexible detector head design that allows for the scintillator arrays to be easily interchanged, thereby facilitating high-sensitivity imaging across a broad energy range (~20 keV to >1 MeV). Another innovation of this system is the use of square MCPMTs that can be easily tiled due to their geometric design. In the future, this approach may be used to create the next generation UCD-SPI system with expanded FOV by tiling together more MCPMTs within the detector heads (e.g. in a 2 × 2 or even a 3 × 3 array) and using a larger scintillator array. This could permit imaging multiple animals simultaneously.

Sensitivity at the CFOV was measured using all detector materials with a wide range of radioisotope energies (table 1). For the NaI(Tl) detectors, sensitivity of 43.7% was measured with ^{109}Cd. As expected, for gamma-ray sources of higher energy, the sensitivity is reduced. With ^{99m}Tc, 31.8% system sensitivity was measured with the NaI(Tl) detectors and 40.2% was measured with the CsI(Na) detectors. Using ^{65}Zn, 2.1% sensitivity was measured with the BGO detectors. All experimental sensitivity and GATE simulation results agree within a few percent. With the system's uniformity and linear response to activity, the system can quantitatively (at the level of ±2%) detect extremely low (~100 nCi) levels of radioactivity (figure 6). This indicates that quantitative measurements of radiolabeled cells *in vitro* could be performed with this system.

The tradeoff of a high-sensitivity single-photon imaging system without collimation is degraded spatial resolution. Using the geometric mean, the best spatial resolution is achieved when the source touches one detector: 19.0 mm for NaI(Tl), 11.9 mm for CsI(Na), and 19.5 mm for BGO (figure 5). (When using only one detector head to image a source distribution close to its face, cm-scale resolution is obtained, but of course at a loss of approximately half of the system sensitivity.) For all scintillator materials, the worst spatial resolution is measured midway between the two detector heads. In the future, the scintillator-to-scintillator spacing can be decreased by eliminating extraneous support/protective material in front of the detector arrays thereby improving the spatial resolution to ~1 cm near one detector face. To demonstrate the improvement in spatial resolution resulting from reduced detector separation, spatial resolution measurements were repeated for the CsI(Na) detectors spaced 15 mm apart and compared to the previous measurements using larger detector spacing of 20 mm. Figure 10 shows the spatial resolution (FWHM) of images formed as the geometric mean of the two CsI(Na) detectors with a capillary tube filled with 1 μCi ^{99m}Tc. As shown, the spatial resolution is much improved with closer detector separation.

The use of the geometric mean is a simple method to produce a single image that combines the data from both detector heads and reduces the depth dependence of the resolution. More sophisticated image reconstruction algorithms are being investigated that could lead to tomographic images [Zhou 2013]. However, a discussion of these approaches is beyond the scope of this manuscript.

In all the examples presented here, the activity is contained within the volume defined by the extent of the detector plates where the sensitivity is fairly uniform. However, as shown in figure 4, the sensitivity drops off rapidly at the edges and is non-zero outside of the FOV defined by the detectors. Thus for extended objects, care needs to be taken to consider these solid angle effects, and any contributions of activity outside of the FOV.

In this work, it has been demonstrated that the high sensitivity and flexible geometry of the UCD-SPI system lends itself to a diverse set of imaging applications. The ^{99m}Tc MAG-3 study showcases the high temporal resolution (even with very low injected doses) and the high sensitivity of the system (approximately one thousand-fold greater than the Siemens Inveon SPECT/CT system, however with far lower spatial resolution and without tomography). The *in vivo* thyroid images in figure 8 illustrate that this system can image the effect of pharmacological interventions, and may be a cost-effective solution to the development and screening of novel drugs and radiotracers. Additionally, the xylem transport images in figure 9 show the capability of plant imaging with the UCD-SPI system; this opens up new opportunities for non-destructively studying gross transport phenomena such as plant response to salt stress or uptake of metals for phytoremediation. These examples are designed to illustrate the rich potential of this very simple and highly sensitive nuclear imaging system for both small animal and plant imaging applications. Although clinical applications for this un-collimated detector imaging approach are limited due to patient size, one translational possibility is in extremity imaging (e.g. wrist or finger imaging) for the assessment of therapy response in patients with arthritis [Chaudhari 2010].

Acknowledgements

This work was supported by the Office of Science (BER), US Department of Energy grant DE-SC0005311. The authors wish to thank Steven Lucero for assistance with system fabrication, Edwin Leung for assistance with the plant experiment, and Dr. Emilie Roncali for many helpful scientific discussions.

References

Acton PD, Kung HF. Small animal imaging with high resolution single photon emission tomography. Nucl. Med. Biol. 2003; 30:889–895. [PubMed: 14698793]

Badr CE, Tannous BA. Bioluminescence imaging: process and applications 2011. Trends in Biotech. 2011; 29:624–633.

Beekman FJ, van der Have F, Vastenhouw B, van der Linden AJA, van Rijk PP, Burbach JPH, Smidt MP. U-SPECT-I: a novel system for submillimeter-resolution tomography with radiolabeled molecules in mice. J. Nucl. Med. 2005; 46:1194–1200. [PubMed: 16000289]

Beekman FJ, van der Have F. The pinhole: gateway to ultra-high-resolution three-dimensional radionuclide imaging. Eur. J. Nucl. Med. Mol. Imaging. 2007; 34:151–161. [PubMed: 17143647]

Bradley EL, Cella J, Majewski S, Popov V, Qian J, Saha MS, Smith MF, Weisenberger AG, Welsh RE. A compact gamma camera for biological imaging. IEEE Trans. Nucl. Sci. 2006; 53:59–65.

Cardis E, et al. Risk of thyroid cancer after exposure to ^{131}I in childhood. J. Natl. Cancer Inst. 2005; 97:724–732. [PubMed: 15900042]

Celler A, Farncombe T, Bever C, Noll D, Maeght J, Harrop R, Lyster D. Performance of the dynamic single photon emission computed tomography (dSPECT) method for decreasing or increasing activity changes. Phys. Med. Biol. 2000; 45:3525–3543. [PubMed: 11131182]

Cherry SR. In Vivo Molecular and Genomic Imaging: New Challenges for Imaging Physics. Phys. Med. Biol. 2004; 49:R13–R48. [PubMed: 15012005]

Chaudhari AJ, Bowen SL, Burkett GW, Packard NJ, Godinez F, Joshi AA, Naguwa SM, Shelton DK, Hunter JC, Boone JM, Buonocore MH, Badawi RD. High-resolution ^{18}F-FDG PET with MRI for monitoring response to treatment in rheumatoid arthritis. Euro. J. Nucl. Med. 2010; 37:1047.

Contag CH, Bachmann MH. Advances in *in vivo* bioluminescence imaging of gene expression. Annu. Rev. Biomed. Eng. 2002; 4:235–260. [PubMed: 12117758]

Currie G, Clarke SJ, Rogers SY, Wheat J. Techniques for technetium scintigraphy in plants. J. Nucl. Med. 2010; 38:76–80.

Erlandsson K, Ivanovic M, Strand S-E, Sjogren K, Weber DA. High resolution pinhole SPECT for small animal imaging. J. Nucl. Med. 1993; 34:9.

Ishizu K, Mukai T, Fujita T, Yonekura Y, Nishizawa S, Tamaki N, Konishi J. Less than 2 mm high resolution SPECT with pinhole collimator for small animals. J. Nucl. Med. 1993; 34:194.

Hammond WT, Bradley EL, Welsh RE, Qian J, Weisenberger AG, Smith MF, Majewski S, Saha MS. A gamma camera re-evaluation of potassium iodide blocking efficiency in mice. Health Phys. 2007; 92:396–406. [PubMed: 17351505]

Jahnke S, Menzel MI, Van Dusschoten D, Roeb GW, Bühler J, Minwuyelet S, Blümler P, Temperton VM, Hombach T, Streun M, Beer S, Khodaverdi M, Ziemons K, Coenen HH, Schurr U. Combined MRI-PET dissects dynamic changes in plant structures and functions. The Plant J. 2009; 59:634–644. [PubMed: 19392708]

Jansen FP, Vanderheyden J. The future of SPECT in a time of PET. Nucl. Med. Biol. 2007; 34:733–752. [PubMed: 17921025]

Jaszczak RJ, Li J, Wang H, Zalutsky MR, Coleman RE. Pinhole collimation for ultra-high-resolution small-field-of-view SPECT. Phys. Med. Biol. 1994; 39:425–437. [PubMed: 15551591]

Judenhofer MS, Pichler BJ, Cherry SR. Evaluation of high performance data acquisition boards for simultaneous sampling of fast signals from PET detectors. Phys. Med. Biol. 2005; 50:29–44. [PubMed: 15715420]

Kenanova V, Barat B, Olafsen T, Chatziioannou A, Herschman HR, Braun J, Wu AM. Recombinant carcinoembryonic antigen as a reporter gene for molecular imaging. Eur. J. Nucl. Med. Mol. Imaging. 2009; 36:104–114. [PubMed: 18719907]

Loudos GK, et al. A 3D high resolution gamma camera for radio pharmaceutical studies with small animals. Appl. Radiat. Isot. 2003; 58:501–508. [PubMed: 12672631]

Magota K, Kubo N, Kuge Y, Nishijima K, Zhao S, Tamaki N. Performance characterization of the Inveon preclinical small-animal PET/SPECT/CT system for multimodality imaging. Eur. J. Nucl. Med. Mol. Imaging. 2011; 38:742–752. [PubMed: 21153410]

Maini CL, Antonacci P, Sargiotto A, Castellano G, Podio V. Dynamic renal scanning using ^{99m}Tc-MAG-3 in man. Eur. J. Nucl. Med. 1989; 15:635–640. [PubMed: 2530091]

Meikle SR, Fulton RR, Eberl S, Dahlbom M, Wong K-P, Fulham MJ. An investigation of coded aperture imaging for small animal SPECT. IEEE Trans. Nucl. Sci. 2001; 48:816–821.

Meikle SR, Kench P, Kassiou M, Banati RB. Small animal SPECT and its place in the matrix of molecular imaging technologies. Phys. Med. Biol. 2005; 50:R45–R61. [PubMed: 16264248]

Mitchell GS, Cherry SR. A high-sensitivity small animal SPECT system. Phys. Med. Biol. 2009; 54:1291–1305. [PubMed: 19190360]

Mu Z, Hong B, Li S, Liu YH. A novel three-dimensional image reconstruction method for near-field coded aperture single photon emission computerized tomography. Med. Phys. 2009; 36:1533–1542. [PubMed: 19544769]

NEMA, NU 1–2007: Performance Measurements of Gamma Cameras.

Roberts J, Chen B, Curtis LM, Agarwal A, Sanders PW, Zinn KR. Detection of early changes in renal function using ^{99m}Tc-MAG3 imaging in a murine model of ischemia-reperfusion injury. Am. J. Physiol. Ren. Physiol. 2007; 293:F1408–F1412.

Rowland D, Cherry S. Small-Animal Preclinical Nuclear Medicine Instrumentation and Methodology. Semin. Nucl. Med. 2008; 38:209–222. [PubMed: 18396180]

van der Have F, Vastenhouw B, Ramakers RM, Branderhorst W, Krah JO, Ji C, Staelens SG, Beekman FJ. U-SPECT-II: An Ultra-High-Resolution Device for Molecular Small-Animal Imaging. J. Nucl. Med. 2009; 50:599–605. [PubMed: 19289425]

Virostko J, Powers AC, Jansen DE. Validation of luminescent source reconstruction using single-view spectrally resolved bioluminescence images. Appl. Opt. 2007; 46:2540–2547. [PubMed: 17429468]

Walker KL, Cherry SR, Mitchell GS. Detector Performance Characterization for High Sensitivity Single-Photon Imaging. IEEE TNS. 2014; 61:1118–1125.

Wang Q, Mathews AJ, Li K, Wen J, Komarov S, O'Sullivan JA, Tai YC. A dedicated high resolution PET imager for plant sciences. 2014 arXiv:1401.3374 [physics.ins-det].

Zinn KR, Chaudhuri TR, Szafran AA, O'Quinn D, Weaver C, Dugger K, Lamar D, Kesterson RA, Wang Z, Frank SJ. Noninvasive Bioluminescence Imaging in Small Animals. ILAR J. 2008; 49:103–115. [PubMed: 18172337]

Zhou, J.; Walker, KL.; Mitchell, GS.; Cherry, SR.; Qi, J. Fully Three-Dimensional Image Reconstruction in Radiology and Nuclear Medicine. Lake Tahoe, California: 2013 Jun 16–21. Maximum *A Posteriori* Image Reconstruction for A High Sensitivity Uncollimated Small-Animal SPECT System; p. 90-93.Retrieved from www.fully3d.org/Fully3D2013Proceedings.pdf Sept. 5, 2014 Print.

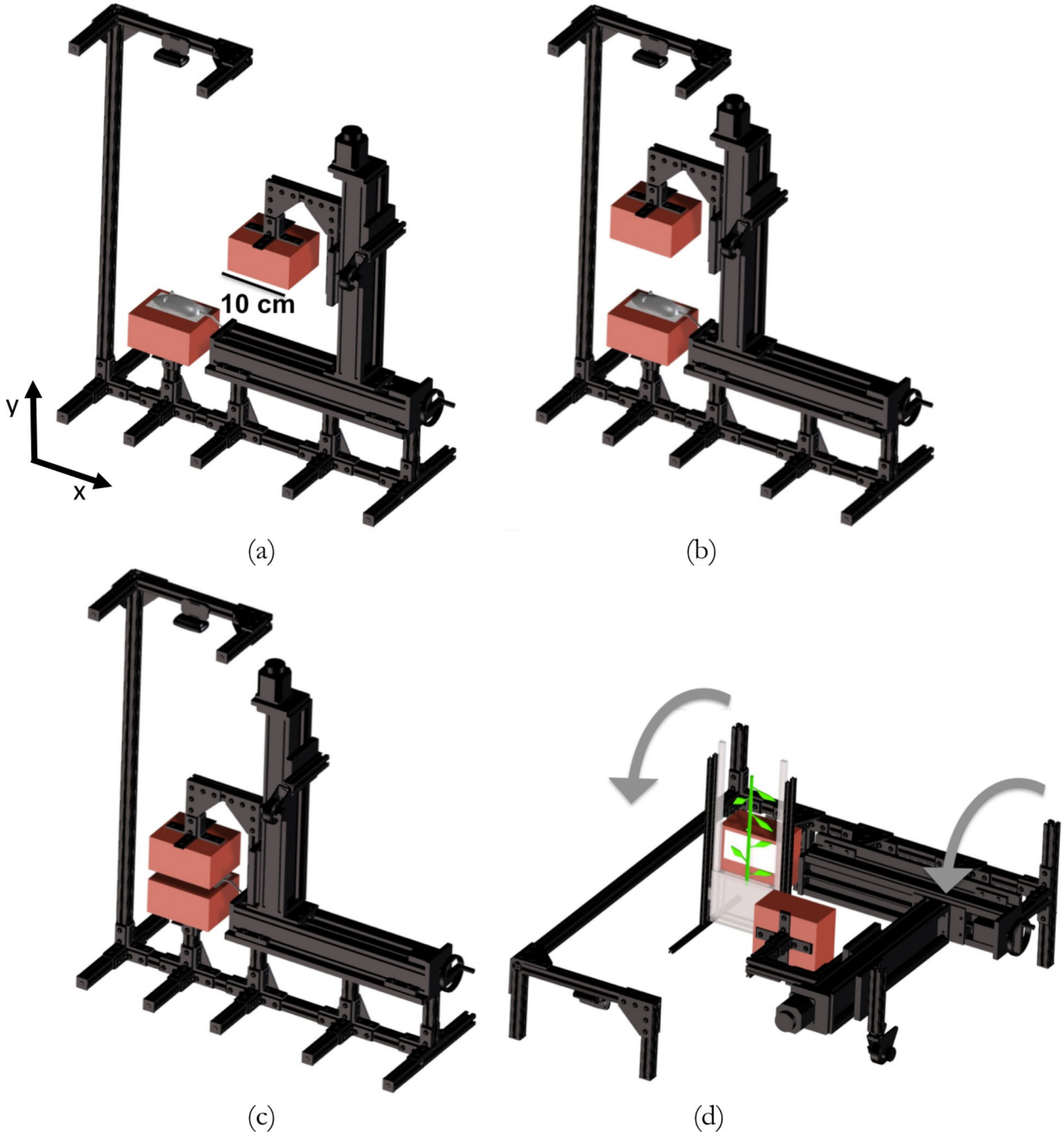

Figure 1.

Conceptual design of the UCD-SPI system for high-sensitivity small animal and plant imaging: (a, b, c) illustration of the dual-axis motion inherent within the design to position the detector heads (shown in red) for small animal imaging; (d) for plant imaging the system can be rotated on its side and a plant moved vertically through the FOV to image its full extent (the detector heads will be directly opposed for plant imaging, representation here is for better visualization).

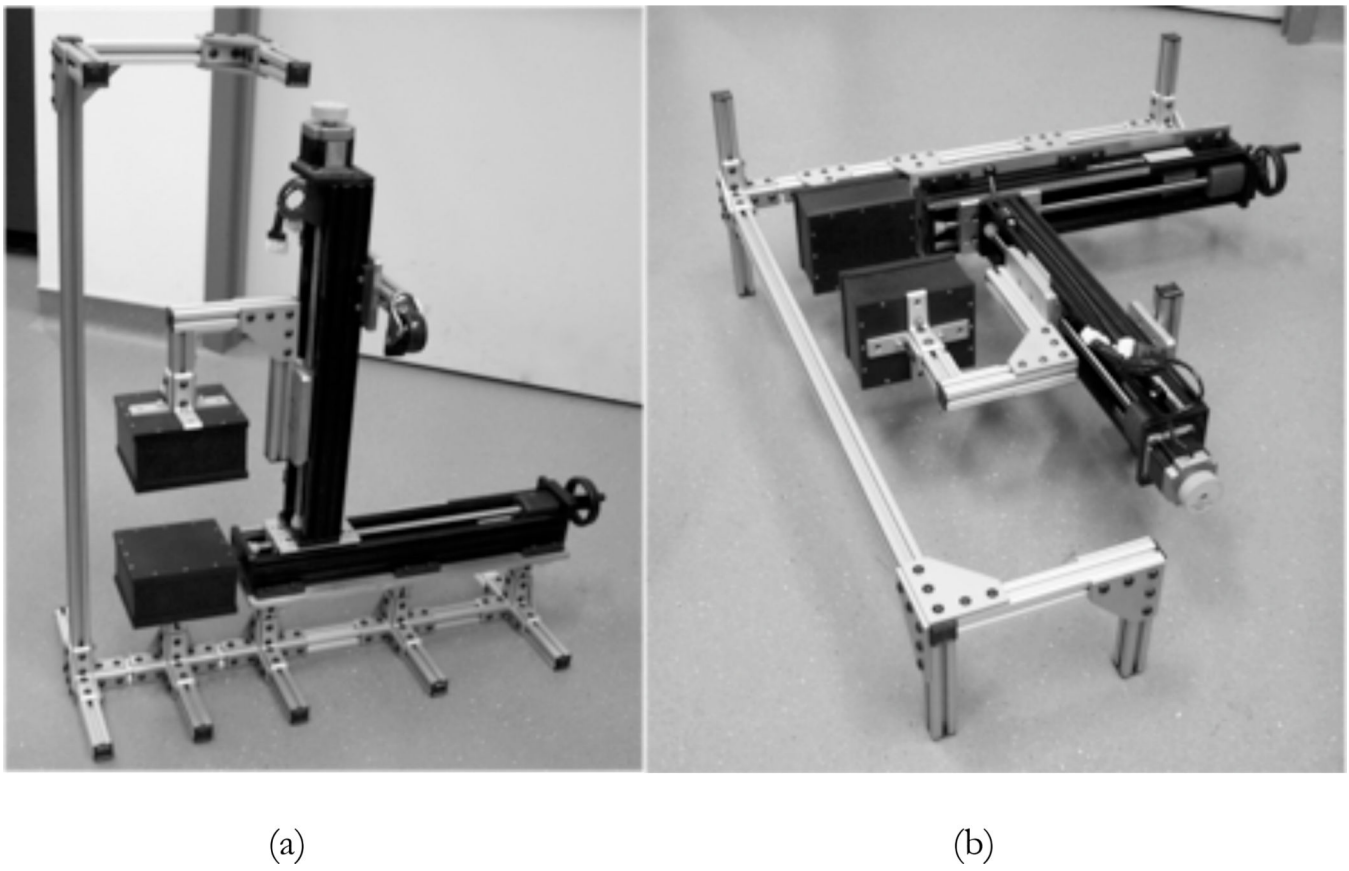

Figure 2.
Photographs of the UCD-SPI system: (a) small animal imaging configuration; (b) plant imaging configuration.

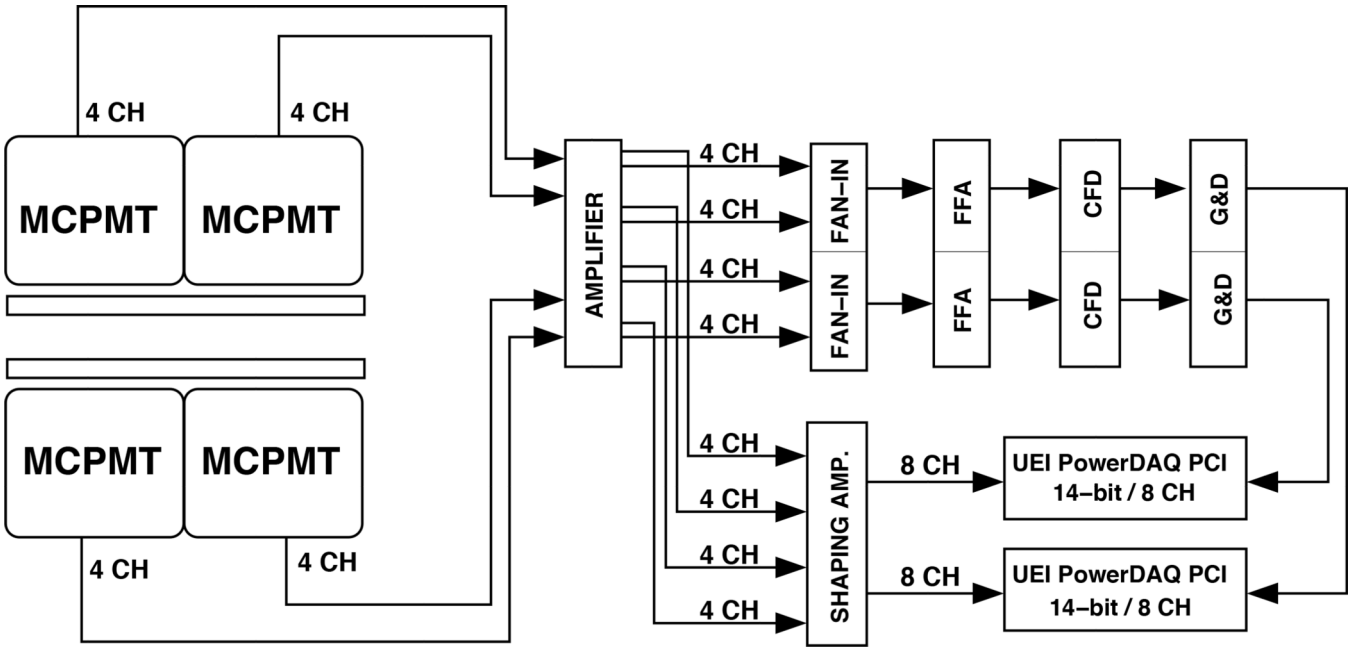

Figure 3.

Schematic of electronics and DAQ for the system. The MCPMTs have four channels each; the eight channels of each detector head are digitized when their sum is over the CFD threshold.

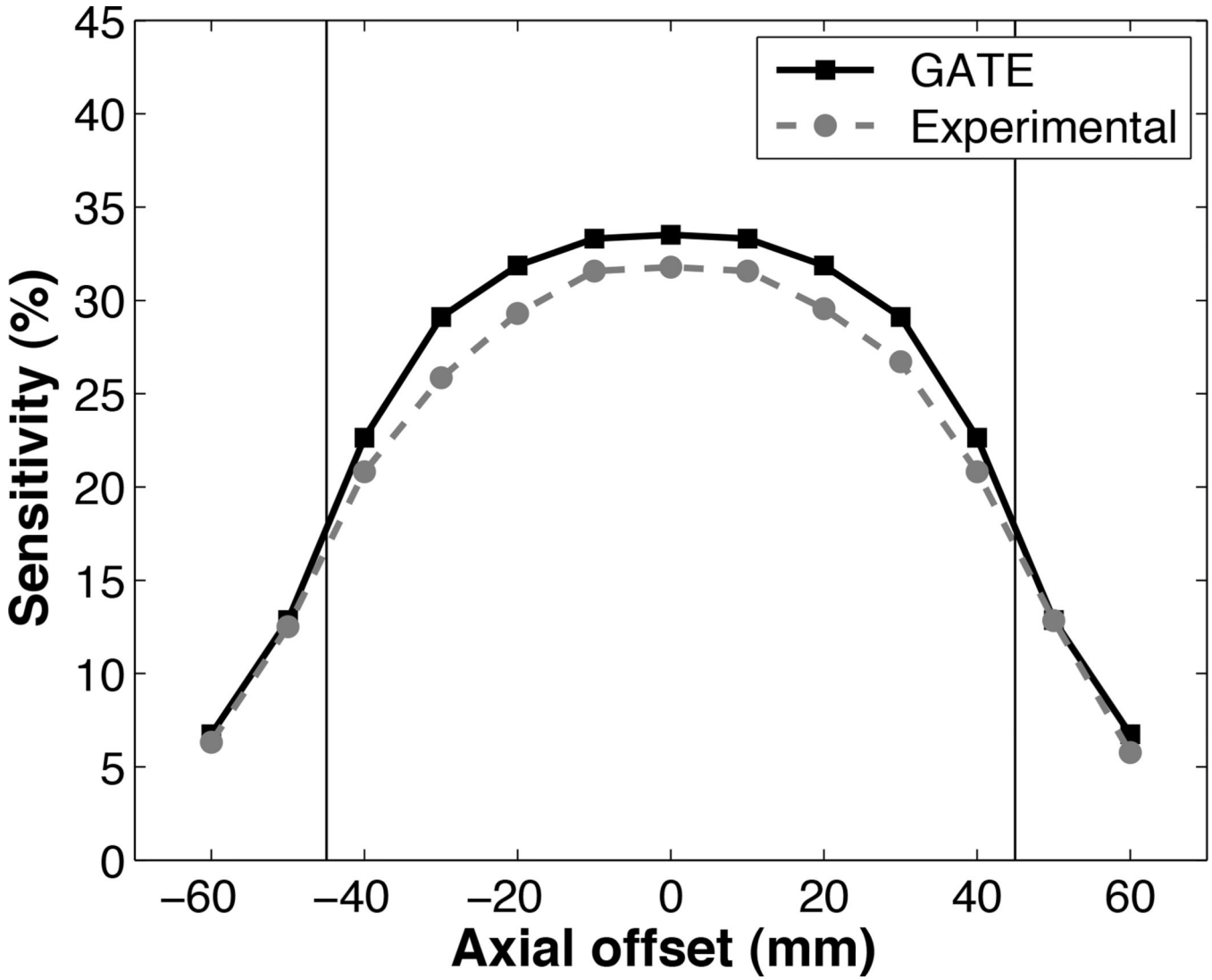

Figure 4.

The sensitivity profile of the UCD-SPI system for ^{99m}Tc (NaI(Tl) detectors) as a function of axial position, the vertical lines at ±45 mm represent the edge of the scintillator array.

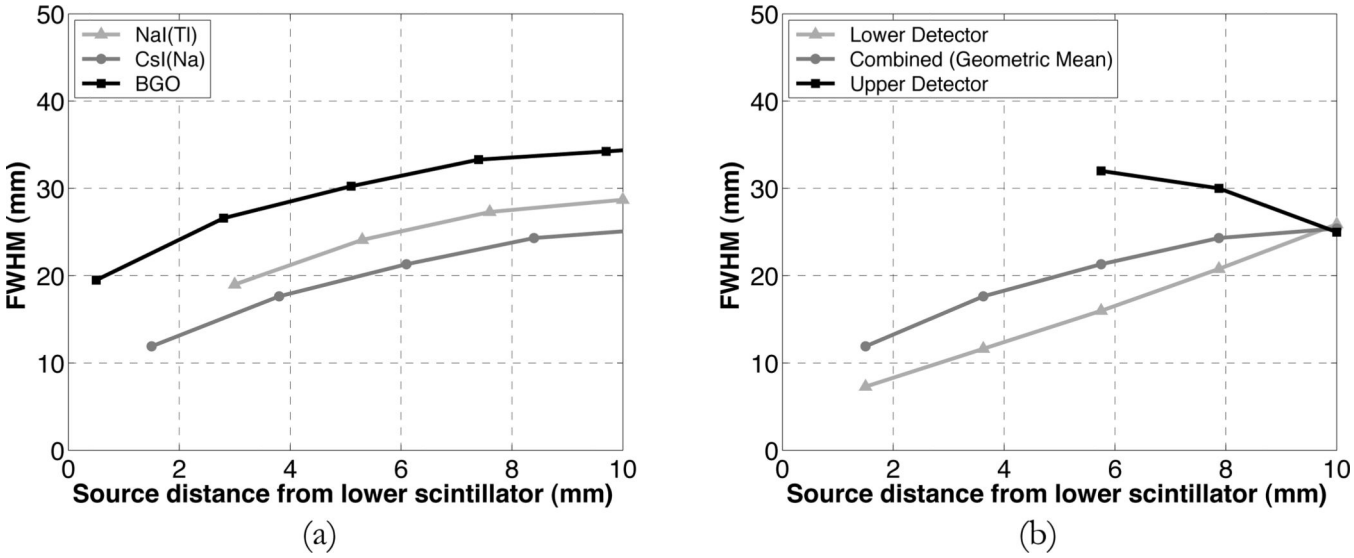

Figure 5.

(a) Spatial resolution (FWHM) of the image formed as the geometric mean of the images from the two detector heads as a function of distance from the entrance face of the lower scintillator. (b) For the CsI(Na) scintillators, the spatial resolution (FWHM) of the combined image is shown alongside measurements from the upper and lower detectors independently (source distance defined with respect to lower detector). All data acquired with a 20 mm separation between entrance faces of scintillator arrays.

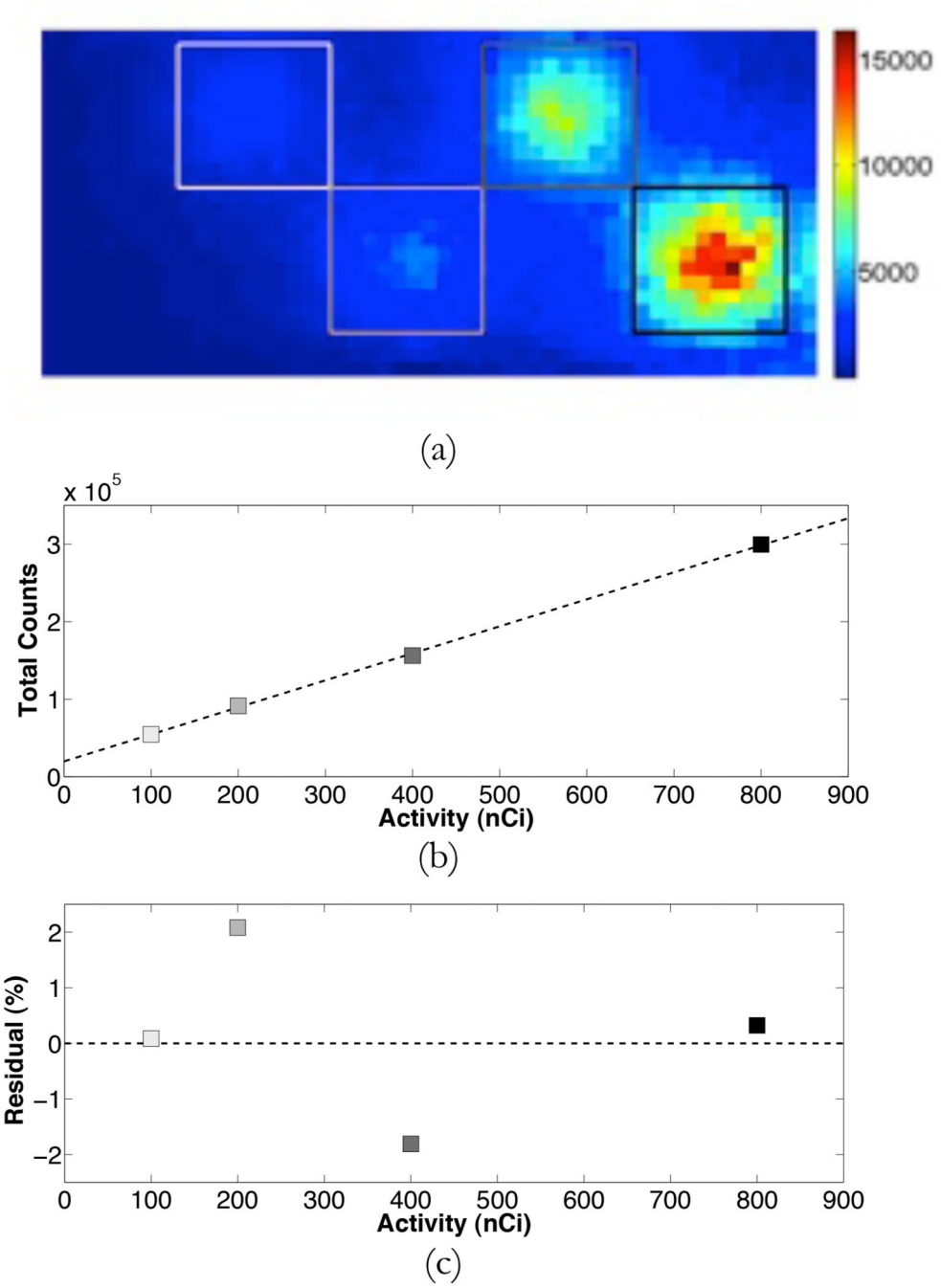

Figure 6.

(a) Projection image of four wells in a 96-well plate filled with trace amounts of ^{99m}Tc solution (100 nCi, 200 nCi, 400 nCi, and 800 nCi). Color scale units are counts per 1.5 mm × 1.5 mm of the NaI(Tl) scintillator detector, per 10 min. (b) A plot of the total number of counts in a 10 × 10 pixel ROI around each filled well. (c) A graph of the % deviation from the best-fit line.

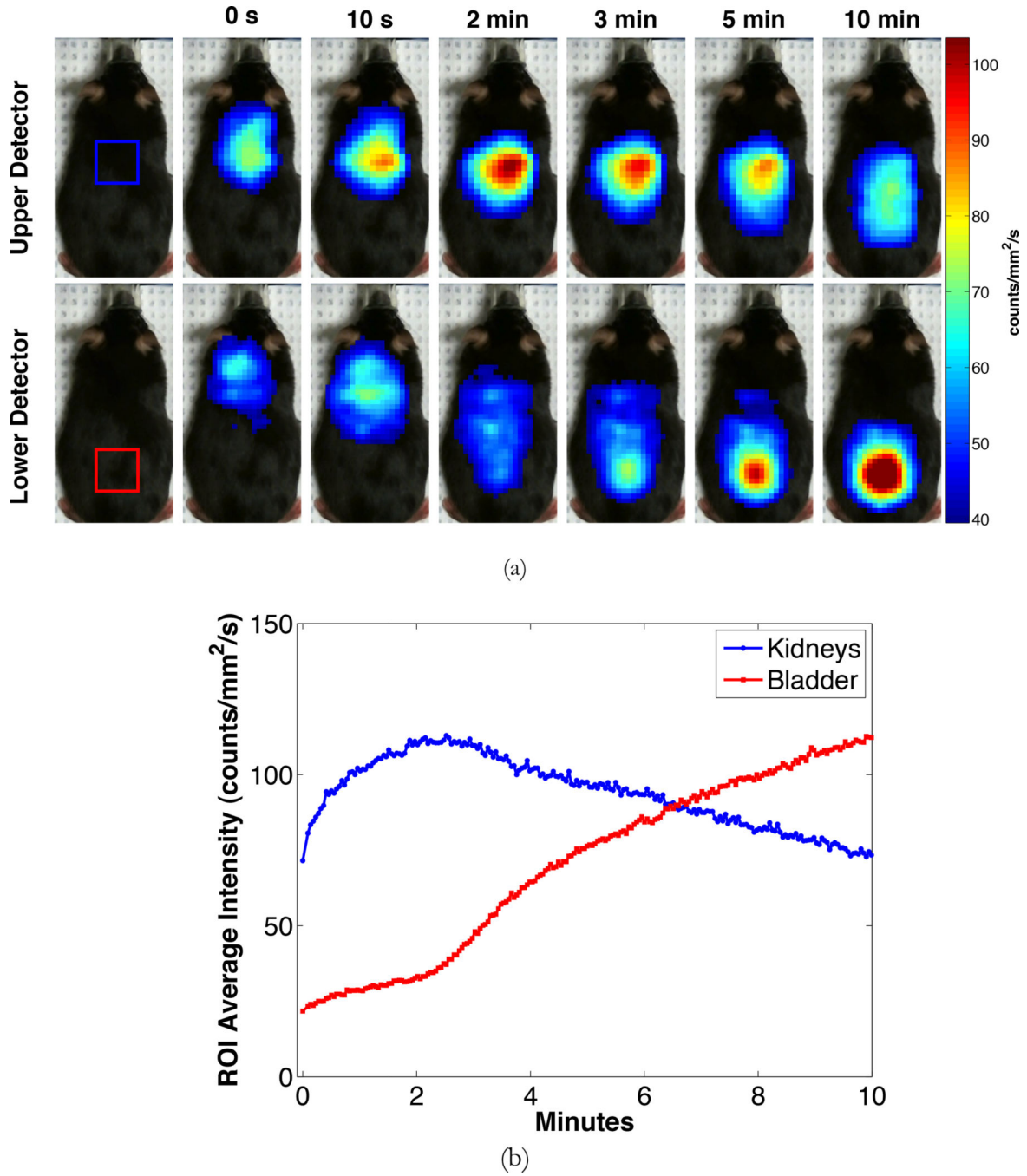

Figure 7.

(a) Six frames (each 2 s long) of a ^{99m}Tc MAG-3 dynamic scan, beginning at 0 s, 10 s, 2 min, 5 min, and 10 min after the end of injection. The thresholded images show a signal from the brain and heart initially, then a signal from the kidneys and finally a signal only from the bladder. Color scale units are counts/mm^2/s. (b) Time-activity curves for the two regions of interest over kidney and bladder as indicated in (a). The units of the ROI average intensity are events per 1 mm^2, averaged over the region of interest, per s, obtained from the image from each detector head.

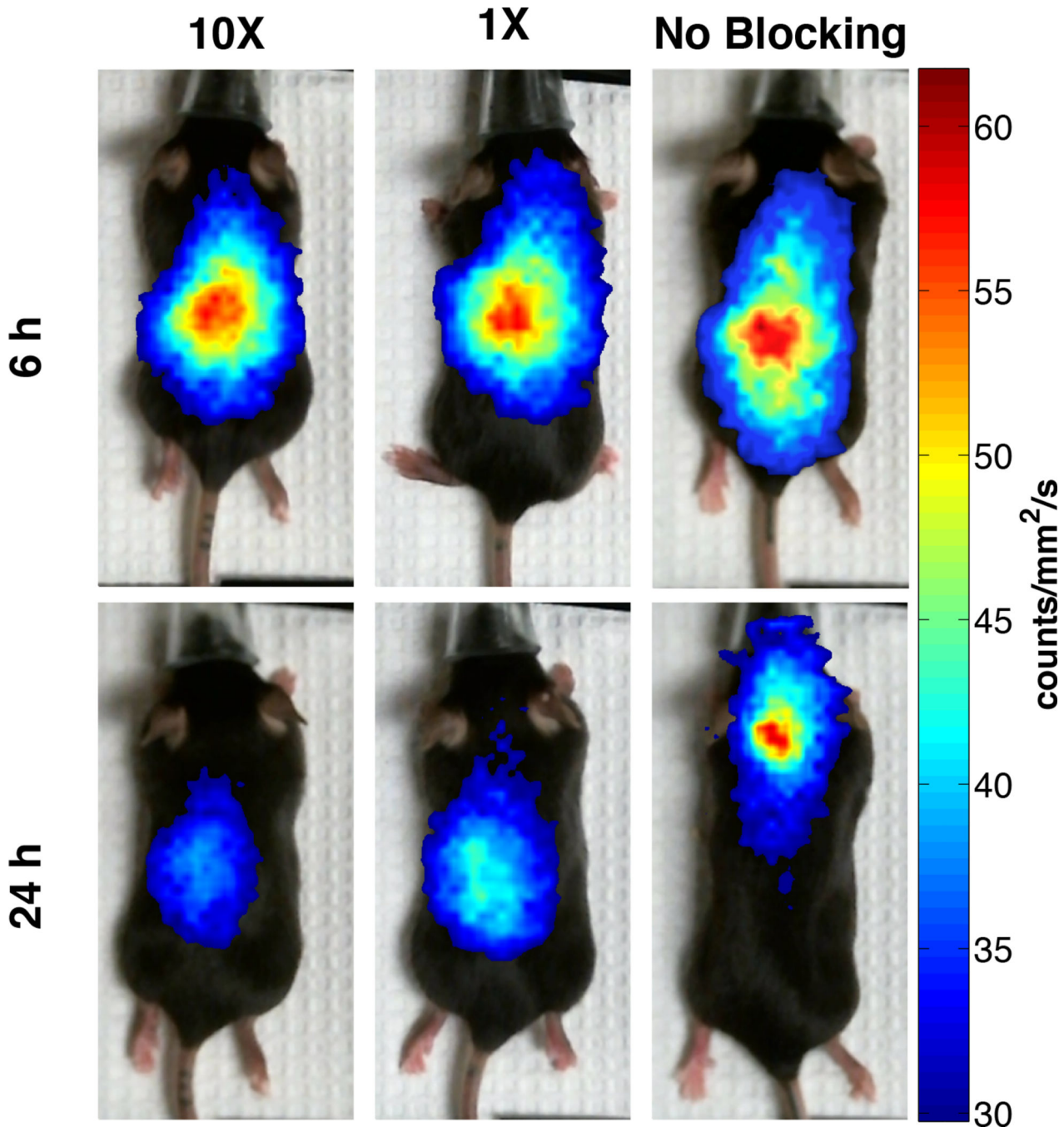

Figure 8.

Co-registered detector data (in thresholded display) overlaid on photographs of the mice at 6 h and 24 h post injection of 3 μCi ^{123}I. At 24 h, radiotracer accumulation in the thyroid occurs only for the mouse that did not receive a blocking dose of KI. Color scale units are counts/mm^2/s.

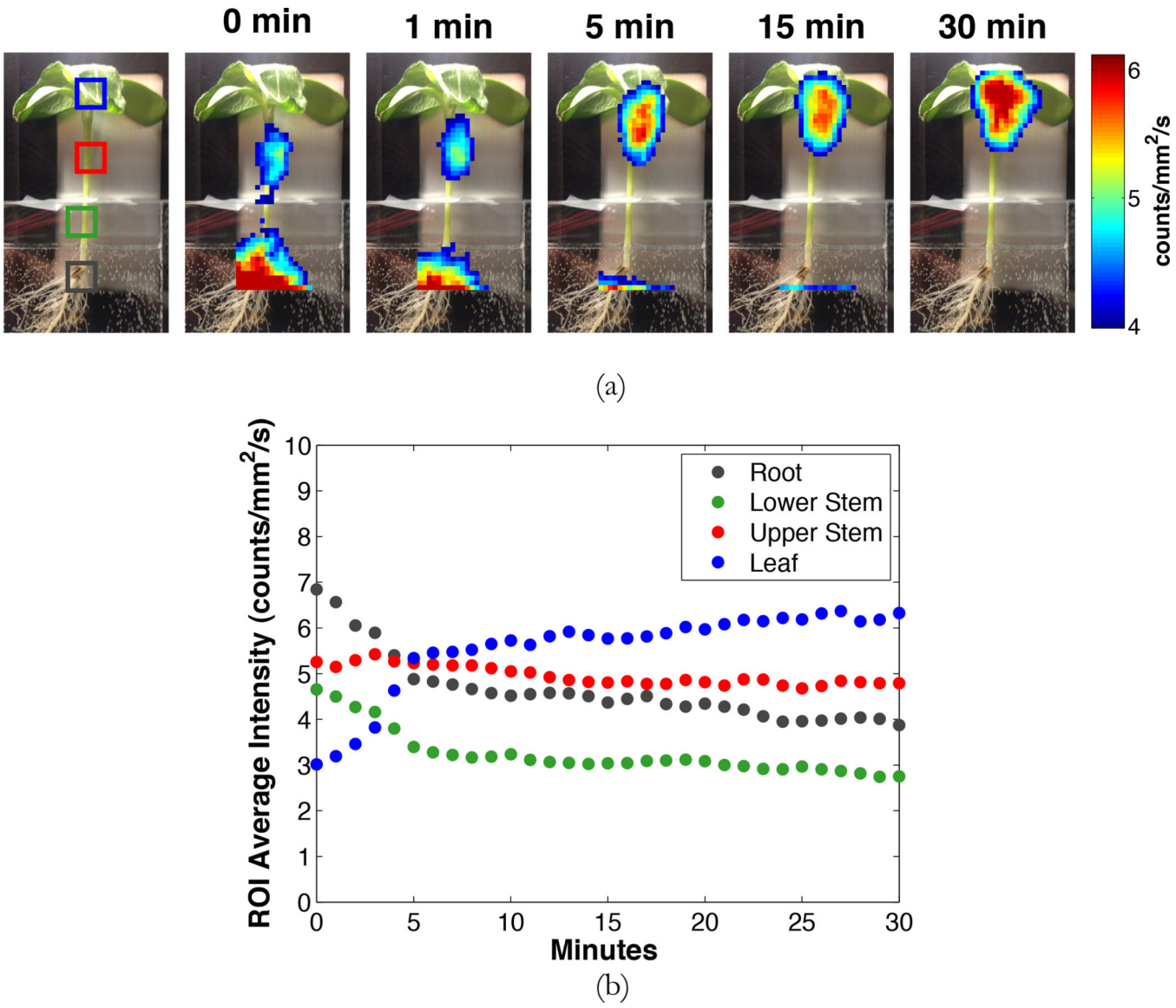

Figure 9.

(a) Five frames (each 45 s long) of a $^{99m}TcO_4^-$ dynamic scan, beginning at 0 min, 1 min, 5 min, 15 min, and 30 min after the end of radioactive incubation and final nutrient water rise. The images show initially a signal from the roots, then a signal from the stem and finally a signal primarily from the leaves. Color scale units are counts/mm^2 /s. (b) Time-activity curves for the four regions of interest indicated in (a). The units of the ROI average intensity are events per mm^2, averaged over the region of interest, per s, obtained from the (non-thresholded) image.

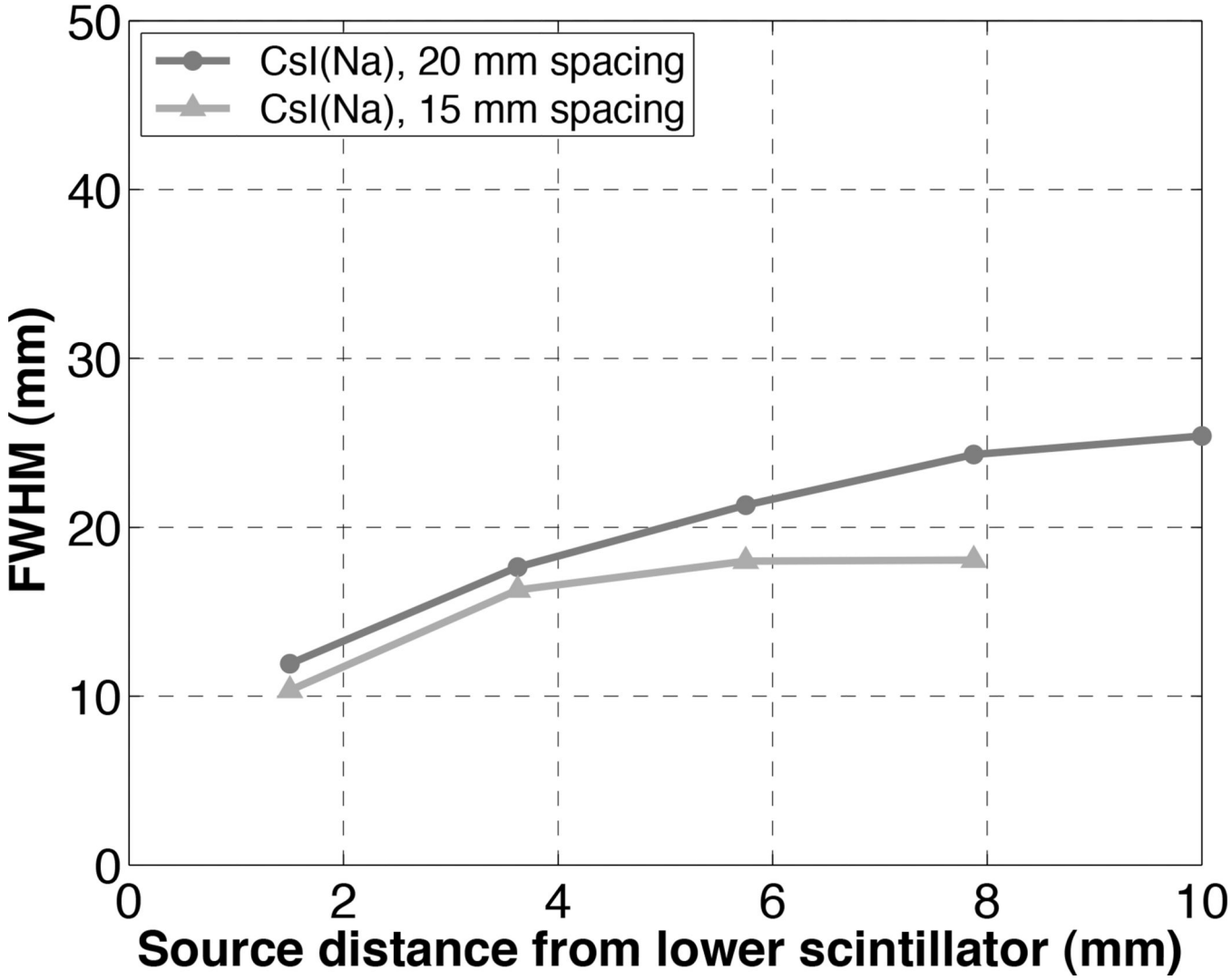

Figure 10.

Spatial resolution (FWHM) of the image formed as the geometric mean of the images from the two CsI(Na) detector heads as a function of the distance from entrance face of the lower scintillator. Detector separation of 20 mm and 15 mm were both investigated.

Table 1

Experimental and GATE sensitivity results at the CFOV.

		Experimental Sensitivity (%)	GATE Sensitivity (%)
NaI(Tl)	^{109}Cd	43.7	46.3
	^{99m}Tc	31.8	33.5
CsI(Na)	^{99m}Tc	40.2	42.6
	^{65}Zn	0.3	0.4
BGO	^{65}Zn	2.1	2.5

Table 2

Integral and differential uniformity measurements for all scintillator materials.

		Uncorrected Uniformity (%)	Corrected Uniformity (%)
NaI(Tl) (122 keV)	Integral	17.6	2.8
	Differential	4.4	0.7
CsI(Na) (122 keV)	Integral	25.6	1.9
	Differential	15.8	0.6
BGO (1116 keV)	Integral	10.1	1.3
	Differential	1.9	0.5